RSC Advances

PAPER

View Article Online
View Journal | View Issue

Cite this: *RSC Adv.*, 2026, **16**, 28507

Early-d-metal Janus MXenes as near-thermoneutral hydrogen evolution electrocatalysts: role of anion identity and d-band asymmetry

Shrestha Dutta and Rudra Banerjee *

Identifying earth-abundant alternatives to platinum for the hydrogen evolution reaction (HER) remains a central challenge in electrocatalysis. Janus MXenes—two-dimensional carbides or nitrides with chemically distinct metal sublattices—break the mirror symmetry of conventional MXenes and create an electronic non-equivalence between the two oxygen-terminated surfaces that is inaccessible in symmetric structures. Here we exploit this asymmetry through a spin-polarised GGA + U density functional theory screening of six O-terminated Janus MXenes $M_1M_2XO_2$ (M_1/M_2 = Ti/Zr, V/Nb, Cr/Mo; X = C, N), constructed as a 3 × 2 factorial series that disentangles d-electron count, 3d/4d orbital extent, and anion electronegativity. Among the thermodynamically stable candidates, only the group-5 VNb pair achieves near-thermoneutral hydrogen binding: $VNbCO_2$ ($\Delta G_{H^*} = -0.03$ eV) and $VNbNO_2$ (−0.11 eV) both satisfy $|\Delta G_{H^*}| \leq 0.3$ eV, whereas the group-4 TiZr systems under-bind and the group-6 CrMo nitride exhibits anomalous under-binding driven by exchange splitting of the Cr d-states. A site-resolved d-band centre analysis reveals that the 3d-metal ε_d correlates strongly with ΔG_{H^*} across the non-magnetic systems ($R = -0.91$) but loses predictive power when spin polarisation is significant. The anion sublattice acts as a secondary compositional lever—shifting ΔG_{H^*} by 0.08 eV within the VNb pair while triggering a 0.67 eV destabilising swing in the magnetic CrMo pair—demonstrating that its tuning capacity is contingent on the metal pair having first placed the system near the volcano apex. These results establish that optimal HER performance in early-d-metal Janus MXenes requires a non-magnetic, spatially asymmetric 3d/4d pair at intermediate d-filling, and identify the VNb combination as a computationally promising candidate for noble-metal-free electrocatalysis.

Received 9th April 2026
Accepted 20th May 2026

DOI: 10.1039/d6ra02989b

rsc.li/rsc-advances

1 Introduction

The efficiency of electrochemical hydrogen production is governed by the strength of hydrogen binding at the catalyst surface. According to the Sabatier principle, an optimal hydrogen evolution reaction (HER) catalyst must bind hydrogen strongly enough to facilitate the Volmer step—proton–electron transfer to the surface—yet weakly enough to permit facile H_2 desorption *via* the Heyrovsky or Tafel pathway.[1] This trade-off is captured by a single thermodynamic descriptor, the Gibbs free energy of hydrogen adsorption (ΔG_{H^*}), which defines a volcano-shaped relationship with the exchange current density; the apex at $\Delta G_{H^*} \approx 0$ marks the thermoneutral optimum.[1,2] Platinum sits near this apex ($\Delta G_{H^*} \approx -0.09$ eV), accounting for its benchmark status,[1] but the scarcity and cost of platinum-group metals preclude their deployment at the terawatt scale demanded by industrial water electrolysis.[3,4] A sustained search for earth-abundant alternatives that satisfy the Nørskov criterion $|\Delta G_{H^*}| \leq 0.3$ eV therefore remains a central challenge in electrocatalysis.[2,4]

Two-dimensional transition-metal carbides and nitrides (MXenes), first synthesised by selective etching of Ti_3AlC_2 in 2011,[5] have attracted considerable attention as candidate HER electrocatalysts.[6,7] With the general formula $M_{n+1}X_nT_x$ (M = early transition metal; X = C or N; T_x = surface termination), MXenes combine metallic conductivity with a hydrophilic, chemically tunable surface.[6,8] Among the accessible terminations, the O-terminated surface is of particular significance for HER because the surface oxygen atoms serve as the primary adsorption centres for hydrogen.[2] Yet this very feature poses a persistent challenge: most O-terminated MXenes bind hydrogen too strongly, yielding $\Delta G_{H^*} \ll 0$ and consequent site poisoning that limits catalytic turnover.[9]

Janus MXenes—structures in which the two outer metal sublattices are occupied by chemically distinct transition metals—offer a route out of this over-binding regime. By breaking the mirror symmetry of the conventional M_2XO_2

Department of Physics and Nanotechnology, SRM Institute of Science and Technology, Kattankulathur, Tamil Nadu, 603203, India. E-mail: rudrab@srmist.edu.in

architecture, the Janus configuration generates an intrinsic out-of-plane dipole and an internal electric field that redistribute charge unevenly between the two metal layers.[10,11] The resulting electronic non-equivalence differentiates the two O-termination sites, creating a site-selective adsorption landscape that is inaccessible in symmetric MXenes.[10] In this context, the site-resolved d-band centre (ε_d)—computed separately for each metal sublattice—regains its utility as a mechanistic descriptor: it captures the very asymmetry that the Janus structure introduces and, as we show below, correlates strongly with the site-dependent ΔG_{H^*} in non-magnetic systems.[6,12] Out-of-plane ordered double-M MAX precursors with two early-d metals on the M-sublattice (*e.g.*, Mo_2TiAlC_2, Mo_2NbAlC_2) are well established experimentally,[8] providing a chemically plausible route to ordered V/Nb Janus monolayers *via* selective etching.

Despite this promise, systematic studies of early d-metal Janus pairs remain limited. Most computational work on bimetallic MXenes has focused on late-transition-metal dopants or on structurally distinct ordered double-transition-metal carbides (*e.g.*, $Mo_2TiC_2O_2$, $Mo_2NbC_2O_2$).[7,12] For the early d-metals of Groups 4, 5, and 6—which are earth-abundant and whose d-orbital chemistry is most amenable to systematic variation—a controlled comparison across metal pairs and, critically, across anion sublattices (carbide *versus* nitride) has not been reported. A complementary ML + DFT screen of ~4500 $M_1M_2XT_2$ compositions at the metal-top adsorption site identifies Nb/Mo/Cr-based O-terminated systems as promising,[13] consistent with our identification of the VNb pair from a much narrower factorial. Our analysis is complementary in treating O-site adsorption and in resolving the spin state explicitly—necessary to capture the exchange-driven failure of the descriptor in $CrMoNO_2$. Whether the anion identity plays a subordinate or decisive role in modulating HER activity in these systems is therefore an open question.

Here we address this gap through a spin-polarised GGA + U density functional theory study of six O-terminated bimetallic Janus MXenes, $M_1M_2XO_2$ (M_1/M_2 = Ti/Zr, V/Nb, Cr/Mo; X = C, N), designed as a 3 × 2 factorial series. By pairing metals from the same periodic group, we hold the valence electron count fixed and isolate the influence of 3d/4d orbital spatial extent; varying the anion then provides an orthogonal compositional axis governed by electronegativity. We evaluate thermodynamic stability through formation energies, characterise the magnetic ground states, quantify Janus electronic asymmetry *via* site-resolved Bader charges and d-band centres, and map the hydrogen adsorption landscape at all inequivalent surface sites. Our results reveal that only the group-5 VNb pair achieves near-thermoneutral hydrogen binding: $VNbCO_2$ (ΔG_{H^*} = −0.03 eV) and $VNbNO_2$ (−0.11 eV) both satisfy $|\Delta G_{H^*}| \leq 0.3$ eV, with the anion sublattice acting as a fine-tuning lever that adjusts binding strength within the thermoneutral window without destabilising the electronic structure. These findings establish computational compositional criteria—intermediate d-filling, quenched magnetism, and 3d/4d spatial asymmetry—for the rational design of Janus MXene HER electrocatalysts.

2 Computational methods

2.1 DFT setup and structural model

All calculations were performed using spin-polarised density functional theory (DFT)[14] with the projector-augmented wave (PAW) method[15] as implemented in the Vienna *Ab initio* Simulation Package (VASP).[16–19] Exchange–correlation effects were described by the Perdew–Burke–Ernzerhof (PBE) functional within the generalised gradient approximation (GGA).[20] To correct for the self-interaction error of localised d-electrons, the rotationally invariant GGA + U scheme of Dudarev *et al.*[21] was applied to every transition-metal site. The effective Hubbard parameters (U_{eff}, in eV) were: Ti 5.0,[22] Zr 3.2,[23] V 3.4,[24] Nb 1.0,[25] Cr 4.0,[26] and Mo 2.0.[27] A plane-wave kinetic-energy cutoff of 520 eV was employed; convergence tests confirmed that increasing the cutoff to 600 eV changed total energies by less than 1 meV per atom.

Each $M_1M_2XO_2$ Janus MXene (M_1/M_2 = Ti/Zr, V/Nb, or Cr/Mo; X = C or N) was modelled as a periodic monolayer with a vacuum spacing of at least 11 Å along the z-axis to decouple periodic images; a dipole correction was applied along z to eliminate residual electrostatic interactions arising from the Janus out-of-plane asymmetry. Brillouin-zone integrations used a Γ-centred 8 × 8 × 1 k-point mesh with first-order Methfessel–Paxton smearing[28] (σ = 0.05 eV), verified to converge total energies to within 1 meV per atom relative to a denser 12 × 12 × 1 mesh. All atomic positions were relaxed until the Hellmann–Feynman forces fell below 0.01 eV $Å^{-1}$. Spin polarisation was enabled throughout; initial magnetic moments of $2\mu_B$ per transition-metal atom were allowed to relax self-consistently.

2.2 Formation energy

Thermodynamic stability was assessed through the formation energy per atom,

$$E_f = \frac{E_{tot} - \sum_i n_i \mu_i}{\sum_i n_i} \quad (1)$$

where E_{tot} is the DFT total energy of the relaxed Janus MXene unit cell, n_i is the number of atoms of species i, and μ_i is the chemical potential of species i taken from the DFT total energy per atom of the elemental standard state (bulk metal or the O_2/N_2/graphite reference, as appropriate). A negative E_f indicates stability against elemental decomposition.

2.3 Gibbs free energy of hydrogen adsorption

HER activity was evaluated within the computational hydrogen electrode (CHE) framework.[1] Hydrogen adsorption was considered at four inequivalent surface sites: the O-termination above M_1 (H@O(M_1)), the O-termination above M_2 (H@O(M_2)), and the two metal top sites H@M_1 and H@M_2. The adsorption energy for each site is

$$\Delta E_{H^*} = E_{slab+H} - E_{slab} - \tfrac{1}{2}E_{H_2}, \quad (2)$$

where E_{slab+H} and E_{slab} are the total energies of the hydrogen-adsorbed and pristine slabs, and E_{H_2} is the total energy of a gas-phase H_2 molecule computed in the same supercell ($E_{H_2} = -6.72$ eV). The Gibbs free energy of adsorption is

$$\Delta G_{H^*} = \Delta E_{H^*} + \Delta ZPE - T\Delta S, \quad (3)$$

where ΔZPE is the zero-point energy correction and $T\Delta S$ the entropic contribution at $T = 298$ K. We adopt the standard empirical values ΔZPE = 0.04 eV and $T\Delta S = 0.40$ eV,[1,29] the latter reflecting the near-complete loss of translational and rotational entropy upon adsorption. This yields $\Delta G_{H^*} = \Delta E_{H^*} - 0.36$ eV. We note that explicit phonon calculations on the adsorbed state would refine these corrections, introducing an uncertainty of ~0.1 eV;[1,30,31] nonetheless, the empirical values are widely validated for comparative screening across structurally related systems.[2,29] Site selection and HER candidacy are assessed independently. The preferred geometry is the configuration of minimum ΔE_{H^*} (site stability, not catalytic optimality); HER candidacy then requires the corresponding ΔG_{H^*} to satisfy $|\Delta G_{H^*}| \leq 0.3$ eV.[1,2,32,33] $TiZrCO_2$, $TiZrNO_2$, and $CrMoNO_2$ are stable but non-catalytic by this test. The full four-site tabulation is in Table S1.

2.4 Bader charge analysis

Site-resolved charge transfer was quantified by Bader charge analysis[34–36] performed on the self-consistent charge densities of all six pristine Janus MXenes using the Henkelman group's grid-based decomposition algorithm.[34] The VASP fine FFT grid (NGXF, NGYF, NGZF set to twice the default values) was used to ensure accurate integration of the Bader volumes. The net charge on each atom is defined as

$$\Delta q_i = q_i^{valence} - q_i^{Bader} \quad (4)$$

where $q_i^{valence}$ is the number of valence electrons in the PAW potential and q_i^{Bader} is the integrated charge within the Bader volume. A positive Δq_i indicates electron donation and a negative value indicates electron accumulation. These site-resolved charges provide a direct measure of the asymmetric charge redistribution between the M_1 and M_2 sublattices that defines the Janus electronic structure.

2.5 D-band centre

The d-band centre (ε_d) was extracted separately for each metal sublattice from the site- and orbital-projected partial density of states (PDOS) obtained *via* the PAW projection scheme (LORBIT = 11). For each metal site, ε_d is the first moment of the spin-summed d-projected DOS relative to the Fermi level:

$$\varepsilon_d = \frac{\int_{E_{min}}^{E_{max}} \varepsilon n_d(\varepsilon) d\varepsilon}{\int_{E_{min}}^{E_{max}} n_d(\varepsilon) d\varepsilon} \quad (5)$$

where $n_d(\varepsilon) = n_d^{\uparrow}(\varepsilon) + n_d^{\downarrow}(\varepsilon)$ is the spin-summed d-projected DOS at energy ε relative to E_F.[37,38] The integration window $[E_{min}, E_{max}]$ = [−10, +6] eV relative to E_F was chosen to encompass the full d-band manifold; extending the window to [−15, +10] eV changed ε_d by less than 0.02 eV. The numerical integration was performed using a Python/NumPy script with a Fermi–Dirac broadening of 0.05 eV. This site-resolved approach is essential for Janus systems, where a single averaged ε_d would obscure the very electronic asymmetry that distinguishes the Janus structure from its symmetric counterpart.

3 Results and discussion

3.1 Crystal structure and thermodynamic stability

The optimised crystal structures of the O-terminated bimetallic Janus MXenes are illustrated in Fig. 1. Each monolayer adopts a hexagonal lattice with five atomic planes stacked along the *z*-direction in the sequence O–M_1–X–M_2–O, where M_1 is the 3d metal (Ti, V, or Cr), M_2 its 4d congener (Zr, Nb, or Mo), and X the anion (C or N). The two surface oxygen layers serve as the primary adsorption sites for hydrogen. Unlike conventional M_2XO_2 MXenes, the Janus configuration places chemically distinct metals on opposite sides of the anion plane, generating an intrinsic out-of-plane dipole that differentiates the two O-termination sites both structurally and electronically.

The optimised lattice parameters are summarised in Table 1. The in-plane lattice constant *a* contracts monotonically from the group-4 TiZr pair ($a = 3.184$ Å for $TiZrCO_2$), through the group-5 VNb pair (3.040 Å), to the group-6 CrMo pair (2.974 Å), tracking the well-known contraction of atomic radii across the early transition-metal series. Replacing C with N generally contracts the lattice—*a* decreases from 3.184 to 3.112 Å in TiZr and from 2.974 to 2.935 Å in CrMo—owing to the shorter and stronger M–N bonds. The VNb system is a marginal exception (3.040 → 3.052 Å), where a subtle vertical registry rearrangement specific to the V/Nb pair slightly expands the basal plane in the nitride.

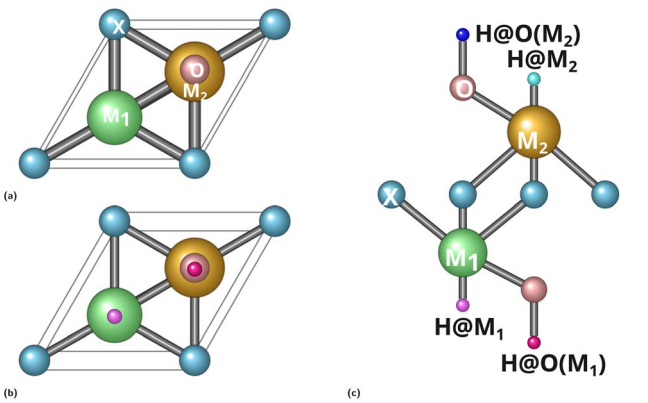

Fig. 1 Crystal structures of the O-terminated bimetallic Janus MXenes ($M_1M_2XO_2$): (a) pristine monolayer, (b) H-adsorbed (top view), and (c) H-adsorbed (side view). The five-layer stacking sequence O–M_1–X–M_2–O is common to all six systems; the broken mirror symmetry is evident from the inequivalent metal sublattices on opposite sides of the anion plane.

Table 1 Optimised in-plane lattice constant (a) and site-resolved net Bader charges (Δq, in $|e|$) for the six Janus MXenes. Positive Δq denotes electron donation; negative values denote electron accumulation. M_1 and M_2 are the 3d and 4d metal sites; X is the anion (C or N); O_{M_1} and O_{M_2} are the oxygen terminations adjacent to M_1 and M_2, respectively. The lattice contracts systematically from group 4 (TiZr) to group 6 (CrMo). In every system the 4d metal donates more charge than its 3d counterpart; this intra-Janus asymmetry increases upon C → N substitution in the VNb pair (from 0.14|e| to 0.19|e|)

System	a (Å)	$\Delta q(M_1)$	$\Delta q(M_2)$	$\Delta q(X)$	$\Delta q(O_{M_1})$	$\Delta q(O_{M_2})$
$TiZrCO_2$	3.184	+2.04	+2.22	−1.87	−1.17	−1.22
$VNbCO_2$	3.040	+1.89	+2.03	−1.77	−1.03	−1.12
$CrMoCO_2$	2.974	+1.68	+1.83	−1.52	−0.96	−1.03
$TiZrNO_2$	3.112	+2.01	+2.22	−1.81	−1.18	−1.24
$VNbNO_2$	3.052	+1.94	+2.13	−1.81	−1.10	−1.16
$CrMoNO_2$	2.935	+1.76	+1.92	−1.63	−1.00	−1.05

The fractional z-coordinates confirm the strictly ordered five-layer vertical sequence in all systems, with unequal M_1–X and X–M_2 interlayer spacings. Taking $CrMoCO_2$ as a structural prototype, the Cr–C spacing is noticeably shorter than the C–Mo spacing, consistent with the more compact 3d orbitals of Cr relative to the spatially extended 4d orbitals of Mo. This vertical asymmetry guarantees a built-in perpendicular dipole—the structural origin of the electronic non-equivalence between the two O-termination sites.

The thermodynamic stability of each Janus MXene, assessed through the formation energy per atom (E_f, Table 2), spans a wide range. The group-4 systems are the most stable: $TiZrCO_2$ ($E_f = -2.76$ eV per atom) and $TiZrNO_2$ (−2.46 eV per atom) benefit from the highly electropositive character of Ti and Zr, which promotes strong ionic bonding. The group-5 systems occupy a moderate stability regime, with the carbide $VNbCO_2$ (−0.85 eV per atom) more stable than the nitride $VNbNO_2$ (−0.36 eV per atom)—consistent with the lower electronegativity of C ($\chi_C = 2.55$) relative to N ($\chi_N = 3.04$), which permits larger net charge transfer and stronger metal–anion bonding in the carbide. Among the group-6 systems, $CrMoCO_2$ has a formation energy of −0.03 eV per atom, within DFT uncertainty and therefore not a reliable indicator of stability against elemental decomposition; we exclude it from the HER candidate set and retain it only as a non-magnetic data point for the ΔG_{H^*} correlation (Section 3.6).

Crucially, the group-5 VNb systems—the principal pair of interest—are both thermodynamically stable ($E_f < 0$) and possess intermediate d-electron counts that, as shown below, place the O-termination electrophilicity in the optimal range for HER.

Formation energies against elemental references provide a necessary but not sufficient stability criterion. The standard next tier of validation—convex-hull analysis against competing phases plus phonon-dispersion or AIMD checks—is recommended in recent authoritative discussions.[39,40] The present filter is intended to identify which members of the 3 × 2 factorial warrant that next-tier investment, and the VNb pair is the primary candidate so identified.

Table 2 Summary of computed properties for the most favoured Janus MXenes. E_f: formation energy per atom (eV per atom); μ: magnetic moment (μ_B per cell); E_{prist}: total energy of the pristine slab (eV); $E_{H@M_i}$ and $E_{H@O(M_i)}$: total energies (eV) with H adsorbed at the M_i metal site or at the O-termination above M_i; ΔG_{H^*}: Gibbs free energy of hydrogen adsorption (eV) at the most favourable site. Carbides are listed above the midline, nitrides below. $VNbCO_2$ and $VNbNO_2$ (bold) are the only systems satisfying $|\Delta G_{H^*}| \leq 0.3$ eV among those that are also thermodynamically stable ($E_f < 0$). The complete table for each configuration and corresponding ΔG_{H^*} is given in SI

System	E_f	μ	E_{prist}	$E_{H@O(M_1)}$	ΔG_{H^*}
$TiZrCO_2$	−2.76	0.00	−44.80	−47.01	+0.79
$VNbCO_2$	−0.85	0.01	−44.90	−47.93	−0.03
$CrMoCO_2$	−0.03	−0.17	−43.65	−46.85	−0.20
$TiZrNO_2$	−2.46	0.00	−46.49	−48.53	+0.96
$VNbNO_2$	−0.36	0.08	−45.66	−48.77	−0.11
$CrMoNO_2$	+0.34	2.67	−44.74	−47.27	+0.47

3.2 Magnetic properties

The calculated magnetic moments (Table 2) reveal a sharp group dependence. The group-4 systems ($TiZrCO_2$, $TiZrNO_2$) are entirely non-magnetic ($0.00\mu_B$), reflecting complete quenching of d-orbital moments by the strongly ionic Ti–O and Zr–O bonding. The group-5 systems are also effectively non-magnetic: $VNbCO_2$ carries a negligible $0.01\mu_B$ and $VNbNO_2$ only $0.08\mu_B$, both quenched by the crystal field and V/Nb d-state hybridisation with the X 2p and O 2p orbitals. A non-magnetic ground state is electronically favourable for HER because spin-degenerate channels at the Fermi level maximise the density of states available for charge transfer during the Volmer step.

The group-6 systems deviate sharply. $CrMoNO_2$ carries a large moment of $2.67\mu_B$, arising from the partially filled Cr d-shell that is insufficiently quenched by hybridisation with Mo. In contrast, $CrMoCO_2$ shows only a weak antiparallel arrangement ($-0.17\mu_B$). This dichotomy reveals that the more electronegative N anion paradoxically preserves greater d-electron localisation on Cr, allowing exchange splitting to develop—a point confirmed by the spin-polarised density of states (Fig. 3), which shows that the moment is spatially localised on the Cr sublattice.

3.3 Charge transfer and Janus electronic asymmetry

The site-resolved Bader charges (Table 1) quantify the charge redistribution that defines the Janus electronic structure. Across all six systems both metal sites act as electron donors, transferring charge to the electronegative anion and surface oxygen layers. A universal pattern emerges: the 4d metal (M_2) donates more charge than its 3d counterpart (M_1) in every case. In $VNbNO_2$, for instance, Nb donates +2.13|e| compared with +1.94|e| for V, yielding an intra-Janus asymmetry of $\Delta(\Delta q) = 0.19|e|$. This difference arises because the spatially extended 4d orbitals of Nb overlap more effectively with the anion and oxygen ligands than the compact 3d orbitals of V, facilitating greater charge transfer despite the near-identical Pauling electronegativities of V ($\chi = 1.63$) and Nb ($\chi = 1.60$). The same trend

holds for TiZr (0.18|*e*| in the carbide, 0.21|*e*| in the nitride) and CrMo (0.15 and 0.16|*e*|).

Anion substitution (C → N) systematically increases the total charge accepted by the anion and oxygen sublattice, consistent with the higher electronegativity of N. In the VNb pair, $\Delta q(\mathrm{N}) = -1.81|e|$ exceeds $\Delta q(\mathrm{C}) = -1.77|e|$, and the oxygen terminations also accumulate slightly more charge in the nitride. Importantly, the intra-Janus charge asymmetry itself increases upon C → N substitution in the VNb pair (from 0.14|*e*| to 0.19|*e*|), demonstrating that the more electronegative anion *amplifies* the Janus electronic non-equivalence. This amplification differentiates the two O-termination sites more strongly, creating a more favourable adsorption environment at the O(M_1) site—a key factor in the superior HER performance of $VNbNO_2$, as demonstrated below.

3.4 Site-dependent hydrogen adsorption

Hydrogen was placed at four inequivalent surface sites on each Janus MXene: H@O(M_1), H@O(M_2), H@M_1, and H@M_2. The total energies and corresponding ΔG_{H^*} values are collected in Table 2. A volcano version showing both H@O(M_1) and H@O(M_2) configurations per system is provided in the supplementary information (Fig. S1).

A notable structural finding is that in $VNbCO_2$ and $VNbNO_2$, hydrogen initially placed on either metal site relaxes spontaneously onto the O-termination during geometry optimisation, without any imposed constraint; in $CrMoCO_2$ the same occurs for H@M_2. For these systems the O-site configuration is not merely the thermodynamic minimum but the *only* stable adsorption geometry accessible from the respective metal-site starting point. In the remaining systems ($TiZrCO_2$, $TiZrNO_2$, and $CrMoNO_2$), H@M_1 and H@M_2 are locally stable but lie well above the H@O energy, confirming the general dominance of O-termination adsorption.[2,7]

For $VNbNO_2$, the preferred H@O(M_1) configuration yields $\Delta G_{H^*} = -0.11$ eV—well within the thermoneutral window. The H@O(M_2) site lies 0.32 eV higher ($\Delta G_{H^*} = +0.21$ eV), a splitting that directly reflects the Janus electronic asymmetry: the V site (M_1) donates less charge than Nb (M_2), leaving the O-termination above V more electron-deficient and hence more electrophilic—the precise environment that strengthens the O–H bond toward thermoneutrality.

The contrast with $VNbCO_2$ isolates the role of the anion sublattice. In the carbide, the lowest-energy O-site gives $\Delta G_{H^*} = -0.03$ eV, essentially thermoneutral within the uncertainty of the empirical thermal correction (∼0.1 eV). Replacing C with N shifts ΔG_{H^*} by −0.08 eV (from −0.03 to −0.11 eV), moving the system further into the exothermic direction while keeping both members of the VNb pair within the low-overpotential regime. The more electronegative N draws additional electron density from the V/Nb bilayer, slightly enriching the O-termination and strengthening the O–H interaction.

The group-4 and group-6 systems bracket this optimum on either side. $TiZrCO_2$ (+0.79 eV) and $TiZrNO_2$ (+0.96 eV) underbind hydrogen: the highly electropositive Ti/Zr metals donate so much charge to the anion sublattice that the O-termination becomes electron-saturated, leaving insufficient electrophilicity to hold H. Counterintuitively, the nitride is *more* underbinding (+0.17 eV shift), because the stronger charge withdrawal by N further depletes the residual metal-layer capacity to activate the surface O.

On the other flank, $CrMoCO_2$ (−0.20 eV) also satisfies $|\Delta G_{H^*}| < 0.3$ eV. However, its marginal thermodynamic stability ($E_f = -0.03$ eV/atom) and the presence of a competing H@O(M_2) site at −0.13 eV—indicating multiple energetically similar configurations that may limit catalytic selectivity—make it a less robust candidate than the VNb pair. $CrMoNO_2$, despite its large magnetic moment and the *a priori* expectation of stronger H binding, shows $\Delta G_{H^*} = +0.47$ eV: the exchange-split Cr d-states paradoxically over-donate charge to the anion sublattice, reducing surface electrophilicity and pushing the system into under-binding territory. The analysis uses the gas-phase isolated-H limit at the CHE level, the established screening protocol for O-terminated MXenes.[1,2,12,13] Solvation and finite-coverage refinements[41–43] are the appropriate next layer for the VNb pair specifically.

3.5 Volcano analysis and compositional trends

The computed ΔG_{H^*} values are plotted on the volcano diagram in Fig. 2a. Three systems fall within the $|\Delta G_{H^*}| \leq 0.3$ eV window: $VNbCO_2$ (−0.03 eV, $\eta = 0.03$ V), $VNbNO_2$ (−0.11 eV, $\eta = 0.11$ V), and $CrMoCO_2$ (−0.20 eV, $\eta = 0.20$ V). The two VNb systems occupy positions nearest the volcano apex, confirming the metal pairing as the decisive compositional variable. Although $CrMoCO_2$ (−0.20 eV) lies nominally inside the window but is disqualified on stability grounds (Section 3.1) and retained only as a mechanistic data point.

Between $VNbCO_2$ and $VNbNO_2$, the carbide sits closer to the apex ($|\Delta G_{H^*}| = 0.03$ *vs.* 0.11 eV), but the 0.08 eV difference is comparable to the inherent uncertainty in the empirical $\Delta ZPE - T\Delta S$ correction (−0.36 eV adopted here; literature values range from −0.24 to −0.40 eV depending on whether system-specific phonon frequencies are used).[1,29] The salient point is therefore that *both* VNb systems lie within the low-overpotential window, whereas all other metal pairs—when combined with thermodynamic stability—do not. The two members represent complementary design targets: $VNbCO_2$ for minimal overpotential, and $VNbNO_2$ where a small exothermic driving force is desirable.

To understand why only the VNb pair achieves this, we trace the two compositional axes independently. Varying the metal pair at fixed N anion gives the progression $\Delta G_{H^*} = +0.96$ ($TiZrNO_2$), −0.11 ($VNbNO_2$), +0.47 eV ($CrMoNO_2$)—a non-monotonic trend reflecting the competing effects of d-electron count and magnetism. The group-4 TiZr pair under-binds because excessive ionicity saturates the surface O; the group-6 CrMo pair in the nitride is unexpectedly *also* under-binding, because the $2.67\mu_B$ exchange-split moment reduces the effective charge available to the O-termination. Only the group-5 VNb pair avoids both extremes.

Varying the anion at fixed metal pair quantifies the C/N tuning lever. For TiZr the shift is +0.17 eV (toward under-

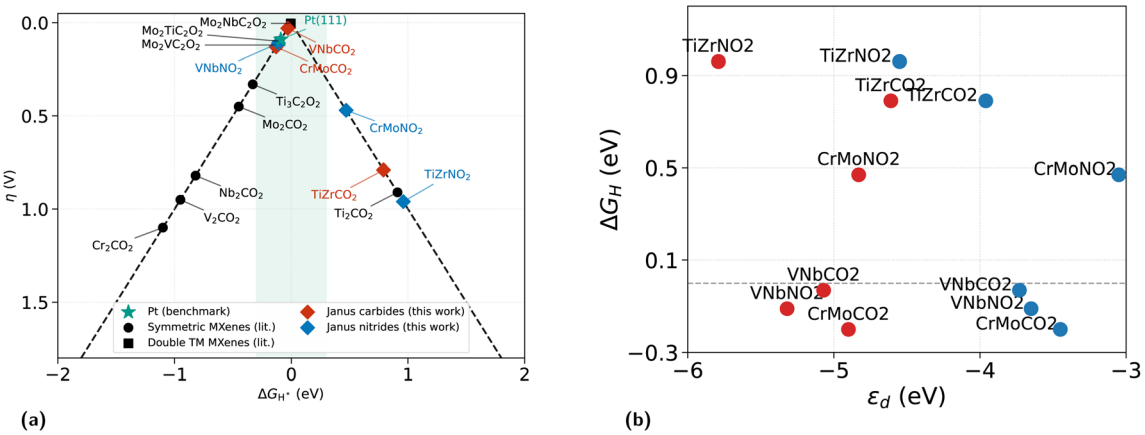

Fig. 2 Variation of ΔG_{H*} with $|\Delta G_{H*}|$ and ε_d. (a) Theoretical HER volcano plot showing the overpotential $\eta = |\Delta G_{H*}|$ as a function of ΔG_{H*} for the six Janus MXenes (filled symbols), alongside literature benchmarks for symmetric O-terminated MXenes (open circles) and ordered double-transition-metal MXenes (open squares). Pt(111) (red star) is shown for reference. The shaded band marks the thermoneutrality window $|\Delta G_{H*}| \leq 0.3$ eV. Both $VNbCO_2$ (−0.03 eV) and $VNbNO_2$ (−0.11 eV) fall inside the window; $CrMoCO_2$ (−0.20 eV) also satisfies the criterion but is marginally stable (see text). (b) ΔG_{H*} *versus* pristine d-band centre ε_d for the 3d (M_1, blue) and 4d (M_2, red) metal sites. Each system appears as a horizontally separated pair at a common ΔG_{H*}; the horizontal gap quantifies the intra-Janus ε_d asymmetry. The dashed line marks $\Delta G_{H*} = 0$. Among the five non-magnetic or weakly magnetic systems, the 3d ε_d correlates strongly with ΔG_{H*} ($R = -0.91$); $CrMoNO_2$ is a clear outlier due to exchange splitting (2.67μ_B).

binding); for VNb it is −0.08 eV (deeper into the window); and for CrMo it is +0.67 eV—a large swing driven by the onset of exchange splitting in $CrMoNO_2$. The anion substitution therefore does not act as a monotonic binding enhancer: its effect is mediated by the magnetic state of the metal pair. VNb is uniquely positioned as the combination where the anion produces only a modest, beneficial adjustment rather than a destabilising swing.

Compared with literature benchmarks (Fig. 2a), symmetric single-metal MXenes (Ti_2CO_2, V_2CO_2, Nb_2CO_2, Cr_2CO_2) all exhibit $|\Delta G_{H*}| > 0.3$ eV at their O-termination sites.[2,7] The ordered double-transition-metal systems $Mo_2VC_2O_2$ and $Mo_2NbC_2O_2$ approach the apex through a structurally distinct three-layer carbide motif and achieve overpotentials comparable to $VNbNO_2$.[12] This equivalence is noteworthy: $VNbNO_2$ matches the HER activity of these structurally complex systems using a simpler two-metal Janus nitride accessible *via* established synthetic routes for Janus monolayers.[10]

3.6 Electronic structure: d-band centre analysis and the origin of thermoneutrality

The site-resolved d-band centres (Fig. 2b) and the spin-polarised DOS (Fig. 3) together provide the electronic foundation for the catalytic trends.

Within every system, the 4d metal (M_2) exhibits a substantially deeper ε_d than the 3d metal (M_1), with intra-Janus differences ranging from 0.65 eV ($TiZrCO_2$) to 1.77 eV ($CrMoNO_2$). This ε_d asymmetry is the electronic fingerprint of the Janus structure—absent by construction in symmetric MXenes—and provides the mechanism through which the two O-termination sites acquire distinct adsorption characteristics. For $VNbNO_2$, the 1.67 eV separation between $\varepsilon_d(V) = -3.65$ eV and $\varepsilon_d(Nb) = -5.32$ eV generates the non-equivalent charge environments responsible for the 0.32 eV difference between H@O(M_1) and H@O(M_2) adsorption energies—a picture corroborated by the Bader charges (Table 1).

The effect of anion substitution on the d-band is most instructive within the VNb pair. Going from $VNbCO_2$ to $VNbNO_2$, ε_d(Nb) shifts downward by 0.25 eV (from −5.07 to −5.32 eV), while ε_d(V) shifts by only +0.08 eV (−3.73 to −3.65 eV, within the numerical integration uncertainty). The pronounced Nb downshift reflects the stronger charge withdrawal by N ($\chi_N = 3.04$) from the spatially extended, more polarisable 4d orbitals; the compact 3d V orbitals are comparatively insensitive to the change in anion electronegativity. This selective depletion deepens ε_d(Nb) and amplifies the charge asymmetry across the Janus bilayer, tipping the O(M_1) termination—above the less-depleted V sublattice—into the electrophilic state that achieves $\Delta G_{H*} = -0.11$ eV.

The CrMo pair shows an anomalous C → N trend. ε_d(Cr) shifts *upward* by 0.40 eV (from −3.45 to −3.05 eV)—the opposite direction from the VNb behaviour. This inversion is a direct consequence of exchange splitting: the 2.67μ_B moment in $CrMoNO_2$ separates the majority- and minority-spin Cr d-bands, pushing the spin-averaged ε_d upward. Far from indicating stronger H binding, this upshift is associated with *reduced* O-site electrophilicity and the positive $\Delta G_{H*} = +0.47$ eV: the exchange-split d-band back-donates charge to the anion sublattice, saturating the surface O and weakening H capture. This constitutes a cautionary example: the d-band centre alone is not a sufficient descriptor in magnetically active Janus systems; the spin state must be treated as a co-descriptor alongside ε_d.

Hydrogen adsorption uniformly upshifts ε_d by 0.3–0.8 eV at both metal sites across all systems, consistent with d-band narrowing as Fermi-level states are consumed by adsorbate bonding. The sole exception is Cr in $CrMoNO_2$ (−0.07 eV

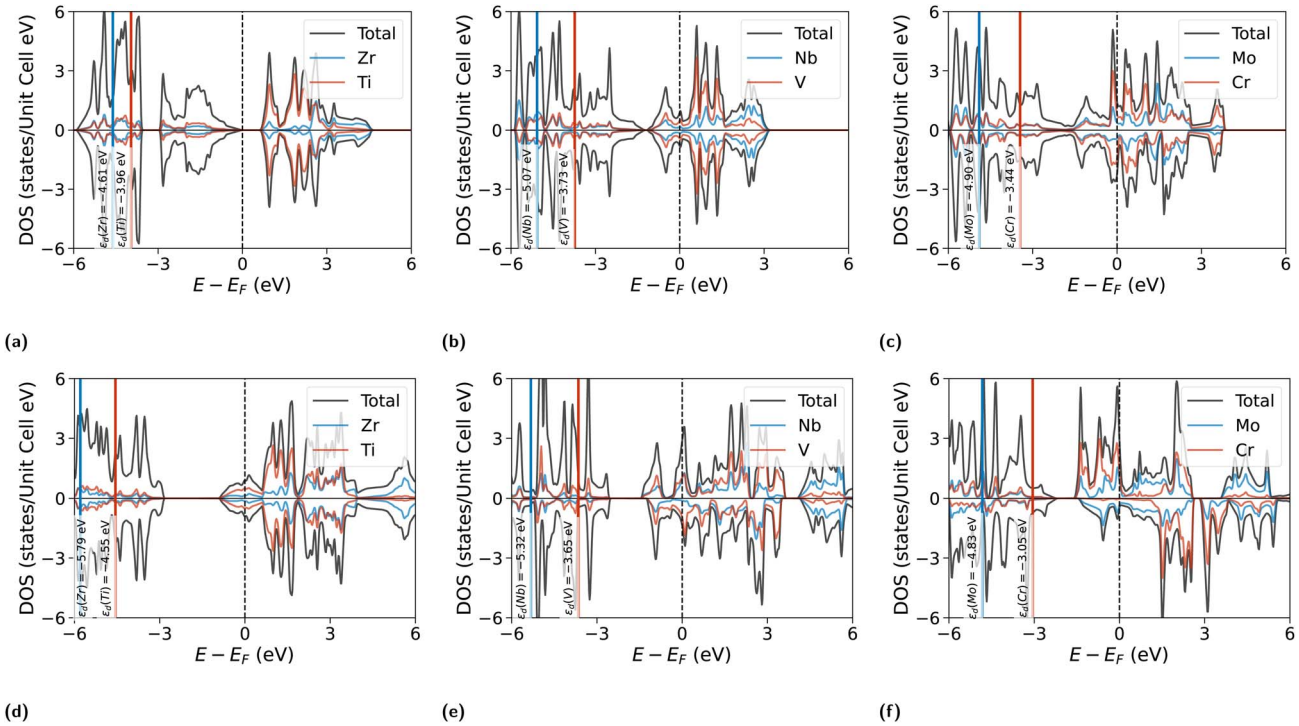

Fig. 3 Spin-polarised total and site-projected partial density of states for the six Janus MXenes. Top row, carbides: (a) $TiZrCO_2$, (b) $VNbCO_2$, (c) $CrMoCO_2$. Bottom row, nitrides: (d) $TiZrNO_2$, (e) $VNbNO_2$, (f) $CrMoNO_2$. Black curves: total DOS; coloured curves: partial contributions from M_1 (3d metal) and M_2 (4d metal). The dashed vertical line marks $E_F = 0$; positive and negative DOS correspond to majority- and minority-spin channels. All six systems are metallic. In $VNbNO_2$ (e) the V and Nb d-band contributions are clearly resolved near E_F, with $\varepsilon_d(V) = -3.65$ eV lying 1.67 eV above $\varepsilon_d(Nb) = -5.32$ eV. $CrMoNO_2$ (f) shows pronounced majority-spin spectral weight from exchange-split Cr d-states ($2.67\mu_B$). Vertical solid lines mark the site-resolved d-band centres $\varepsilon_d(M_1)$ and $\varepsilon_d(M_2)$, with values labelled adjacent.

downshift), attributable to exchange-splitting rearrangement. The consistency of this adsorption-induced upshift in all non-magnetic and weakly magnetic systems validates the pristine ε_d as the relevant descriptor for inter-system comparisons.

The correlation between pristine ε_d and ΔG_{H^*} is visualised in Fig. 2b. For the 3d metal sites, a strong negative correlation ($R = -0.91$, excluding the magnetic $CrMoNO_2$) connects ε_d to ΔG_{H^*}: deeper d-band centres correspond to weaker binding, reflecting reduced d-electron availability near E_F for activating the O-termination. The 4d metal sites show a weaker correlation ($R = -0.18$), consistent with the indirect influence of the subsurface M_2 layer on the H-adsorbing O-site. $CrMoNO_2$ deviates markedly on both panels—its Cr ε_d of -3.05 eV is the shallowest in the series, which by the non-magnetic trend should predict strong over-binding, yet its ΔG_{H^*} is positive. This confirms that the spin-averaged ε_d loses its predictive power when significant spin polarisation is present. The detailed table is added in SI.

3.7 Mechanistic picture and design principles

The analyses above establish a coherent mechanistic picture. The VNb group-5 pair provides the appropriate d-electron count to place the O-termination near the optimal electrophilicity threshold. The anion sublattice acts as a fine-tuning lever within this pair: the more electronegative N selectively deepens ε_d(Nb) and amplifies the Janus charge asymmetry ($0.19|e|$ in the nitride *vs.* $0.14|e|$ in the carbide) without destabilising the electronic structure or triggering exchange splitting. Neither the TiZr pair (excessive ionicity) nor the CrMo pair (magnetic instability) can achieve this balance.

Three design criteria therefore emerge for Janus MXene HER catalysts: (i) an intermediate d-electron count (group 5) that avoids both excessive ionicity and exchange splitting; (ii) a quenched magnetic moment ensuring spin-degenerate Fermi-level channels for efficient charge transfer; and (iii) iso-electronegative yet spatially asymmetric 3d/4d metal sites that generate the charge non-equivalence necessary for site-selective O-termination adsorption.

The anion sublattice is a secondary handle in non-magnetic metal pairs (C → N shifts ΔG_{H^*} by 0.08 eV in VNb), and a decisive one when it alters the surface magnetic state: in CrMo, C → N triggers a $2.67\mu_B$ moment on Cr and a 0.67 eV swing that ejects the nitride from the thermoneutral window.

4 Conclusions

By screening six O-terminated bimetallic Janus MXenes across a controlled 3×2 factorial design, we have shown that a single compositional variable—the metal-pair identity—determines whether a Janus MXene can access the thermoneutral hydrogen-binding regime. Of the three same-group 3d/4d pairs examined, only the group-5 VNb combination satisfies both prerequisites for a viable HER electrocatalyst: thermodynamic stability ($E_f < 0$)

and near-zero ΔG_{H^*} (−0.03 and −0.11 eV for the carbide and nitride, respectively). The group-4 TiZr pair fails on the over-ionic side; the group-6 CrMo pair fails because exchange splitting in the nitride disrupts the d-band–ΔG_{H^*} correlation that governs the non-magnetic systems ($R = -0.91$).

The origin of the VNb optimum is electronic rather than structural. Pairing metals from the same group holds the valence electron count fixed, so the Janus asymmetry arises entirely from the 3d/4d orbital-extent mismatch. This mismatch generates a site-resolved ε_d splitting of 1.67 eV, which differentiates the two O-termination sites and places one of them at the electrophilicity threshold required for thermoneutral H binding. The anion sublattice then provides an orthogonal tuning axis: C *versus* N shifts ΔG_{H^*} by 0.08 eV within the VNb pair—a modest adjustment that keeps both systems inside the low-overpotential window—while the same substitution destabilises the CrMo pair by 0.67 eV through magnetic onset. The anion is therefore a secondary lever in non-magnetic pairs and a decisive variable when its substitution alters the surface magnetic state.

These findings distil into a concise design rule: optimal HER performance in Janus MXenes requires intermediate d-filling, quenched magnetism, and 3d/4d spatial asymmetry at matched electronegativity—conditions met uniquely by the VNb pair in the early d-metal series. We note that the empirical zero-point and entropy corrections used here carry an uncertainty of ∼0.1 eV; phonon calculations on the adsorbed state would sharpen the quantitative distinction between the carbide and nitride.

Experimental verification of V/Nb layering during selective etching and of V^{4+}/Nb^{4+} preservation under HER conditions lies outside this computational screening and is required before the VNb pair can be advanced as a true synthetic target. Phonon-dispersion and constant-temperature AIMD validation of the VNb pair under HER conditions constitutes the principal computational next step. More broadly, the factorial screening strategy demonstrated here—orthogonal variation of metal pair and anion—offers a transferable template for navigating the high-dimensional compositional space of Janus MXenes toward targeted catalytic function.

Author contributions

Shrestha Dutta: writing – original draft, visualization, validation, investigation, data curation. Rudra Banerjee: writing – review & editing, validation, supervision, methodology, formal analysis, conceptualization.

Conflicts of interest

There are no conflicts to declare.

Data availability

Data will be made available on request. Supplementary information (SI): Gibbs energy, Bader charge density and analysis of all 6 systems. See DOI: https://doi.org/10.1039/d6ra02989b.

Acknowledgements

We express our sincere gratitude to the high performance computing center (HPCC), SRMIST and the Department of Physics and Nanotechnology for their support of the computational facility. We are appreciative of the computational resource provided by the National Supercomputing Mission (NSM, CDAC), Government of India. We also express our heartiest gratitude to Selective Excellence Research Initiative (SERI), SRMIST for their support in our research work. We have used LLM for cleanup and correction of text.

References

1 J. K. Nørskov, T. Bligaard, A. Logadottir, J. R. Kitchin, J. G. Chen, S. Pandelov and U. Stimming, *J. Electrochem. Soc.*, 2005, **152**, J23–J26.
2 C. Ling, L. Shi, Y. Ouyang and J. Wang, *Chem. Mater.*, 2016, **28**, 9026–9032.
3 U. Arshad, J. Tang and Z. Shao, *SusMat*, 2025, **5**, e267.
4 M. A. Qadeer, X. Zhang, M. A. Farid, M. Tanveer, Y. Yan, S. Du, Z.-F. Huang, M. Tahir and J.-J. Zou, *J. Power Sources*, 2025, **613**, 234856.
5 M. Naguib, M. Kurtoglu, V. Presser, J. Lu, J. Niu, M. Heon, L. Hultman, Y. Gogotsi and M. W. Barsoum, *Adv. Mater.*, 2011, **23**, 4248–4253.
6 J. Hu, J. Mo, C. Yu, D. Liu, R. Zhang, L. Miao, X. Ji and J. Jiang, *Appl. Surf. Sci.*, 2024, **653**, 159329.
7 M. Mocelim, P. I. Rodrigues Moraes, R. L. H. Freire and J. L. F. Da Silva, *J. Phys. Chem. C*, 2026, **130**, 217–230.
8 Y. Gogotsi and B. Anasori, *ACS Nano*, 2019, **13**, 8491–8494.
9 S. A. Sergiienko, A. V. Kovalevsky, J. Luxa, K. Mosina, B. Wu, G. Constantinescu, J. Azadmanjiri, N. D. Shcherban, O. Diyuk and Z. Sofer, *RSC Adv.*, 2025, **15**, 43505–43522.
10 A.-Y. Lu, H. Zhu, J. Xiao, C.-P. Chuu, Y. Han, M.-H. Chiu, C.-C. Cheng, C.-W. Yang, K.-H. Wei, Y. Yang, Y. Wang, D. Sokaras, D. Nordlund, P. Yang, D. A. Muller, M.-Y. Chou, X. Zhang and L.-J. Li, *Nat. Nanotechnol.*, 2017, **12**, 744–749.
11 H. Huang, X. Liu, L. Sun, Z. Shang, T. Zhou, P. Li and B. Wu, *Coatings*, 2025, **15**, 580.
12 J. Du, Y. Yan, X. Li, J. Chen, C. Guo, Y. Chen and H. Wang, *Chem. Sci.*, 2025, **16**, 9424–9435.
13 B. M. Abraham, P. Sinha, P. Halder and J. K. Singh, *J. Mater. Chem. A*, 2023, **11**, 8091–8100.
14 S. Kurth, M. A. L. Marques and E. K. U. Gross, *Encyclopedia of Condensed Matter Physics*, Elsevier, Oxford, 2005, pp. 395–402.
15 P. E. Blöchl, *Phys. Rev. B: Condens. Matter Mater. Phys.*, 1994, **50**, 17953–17979.
16 G. Kresse and J. Hafner, *Phys. Rev. B: Condens. Matter Mater. Phys.*, 1993, **47**, 558–561.
17 G. Kresse and J. Hafner, *Phys. Rev. B: Condens. Matter Mater. Phys.*, 1994, **49**, 14251–14269.
18 G. Kresse and J. Furthmüller, *Phys. Rev. B: Condens. Matter Mater. Phys.*, 1996, **54**, 11169–11186.

19 G. Kresse and D. Joubert, *Phys. Rev. B: Condens. Matter Mater. Phys.*, 1999, **59**, 1758–1775.
20 M. Ernzerhof and G. E. Scuseria, *J. Chem. Phys.*, 1999, **110**, 5029–5036.
21 S. L. Dudarev, G. A. Botton, S. Y. Savrasov, C. J. Humphreys and A. P. Sutton, *Phys. Rev. B*, 1998, **57**, 1505–1509.
22 N. Garcia-Romeral, A. Morales-Garcia, F. Vines, I. d. P. R. Moreira and F. Illas, *Phys. Chem. Chem. Phys.*, 2023, **25**, 17116–17127.
23 S. Rahimi, E. H. Semiromi and A. Mostafaei, *Sci. Rep.*, 2025, **15**(1), 21690.
24 B. Stahl and T. Bredow, *J. Comput. Chem.*, 2020, **41**, 258–265.
25 A. O'Hara, T. N. Nunley, A. B. Posadas, S. Zollner and A. A. Demkov, *J. Appl. Phys.*, 2014, **116**, 213705.
26 S. Pakdel, T. Olsen and K. S. Thygesen, *npj Comput. Mater.*, 2025, **11**, 2057–3960.
27 Q. Cai, R. Xu, T. Wang, L. Niu, Y. Gong and C. Li, *iScience*, 2025, **28**, 112762.
28 M. Methfessel and A. T. Paxton, *Phys. Rev. B*, 1989, **40**, 3616–3621.
29 P. Sen, K. Alam, T. Das, R. Banerjee and S. Chakraborty, *J. Phys. Chem. Lett.*, 2020, **11**, 3192–3197.
30 Z. Sun, R. Li, Q. Xi, F. Xie, X. Jian, X. Gao, H. Li, Z. Yu, J. Liu, X. Zhang, Y. Wang, Y. Wang, X. Yue and C. Fan, *Phys. Chem. Chem. Phys.*, 2023, **25**, 13728.
31 M. V. Jyothirmai, D. Roshini, B. M. Abraham and J. K. Singh, *ACS Appl. Energy Mater.*, 2023, **6**, 5598–5606.
32 J. Mou, Y. Gao, J. Wang, J. Ma and H. Ren, *RSC Adv.*, 2019, **9**, 11755.
33 M. V. Jyothirmai, R. Dantuluri, P. Sinha, B. M. Abraham and J. K. Singh, *ACS Appl. Mater. Interfaces*, 2024, **16**, 12437–12445.
34 G. Henkelman, A. Arnaldsson and H. Jónsson, *Comput. Mater. Sci.*, 2006, **36**, 354–360.
35 W. Tang, E. Sanville and G. Henkelman, *J. Phys.: Condens. Matter*, 2009, **21**, 084204.
36 E. Sanville, S. D. Kenny, R. Smith and G. Henkelman, *J. Comput. Chem.*, 2007, **28**, 899–908.
37 B. Hammer and J. K. Nørskov, *Advances in Catalysis*, Academic Press, 2000, vol. 45, pp. 71–129.
38 B. Hammer and J. K. Nørskov, *Nature*, 1995, **376**, 238–240.
39 Z. Zeng, X. Chen, K. Weng, B. Jiang, P. Lian, W. Huang and W. Hu, *npj Comput. Mater.*, 2021, **7**, 80.
40 P. Varma, S. Saha, N. K. Banoth, A. N. Chokkapu, S. J. Lee, B. M. Abraham, D. A. Reddy and U. Pal, *J. Mater. Chem. A*, 2026, **14**, 14788–14853.
41 Z. Shu, Z. Shi, M.-F. Ng, T. Tan and Y. Cai, *Materials Today Sustainability*, 2024, **26**, 100808.
42 J. Du, Y. Yan, X. Li, J. Chen, C. Guo, Y. Chen and H. Wang, *Chem. Sci.*, 2025, **16**, 9424–9435.
43 P. Wan, Y. Chen and Q. Tang, *ChemPhysChem*, 2024, **25**, e202400325.